Acta Oceanol. Sin., 2022, Vol. 41, No. 2, P. 127–138
https://doi.org/10.1007/s13131-021-1849-4
http://www.aosocean.com
E-mail: ocean2@hyxb.org.cn

Numerical investigation of the control factors driving Zhe-Min Coastal Current

Yang Zhang[1, 2], Fei Chai[1, 3*], Joseph Zhang[4], Yang Ding[5], Min Bao[1], Yunwei Yan[1], Hong Li[6], Wei Yu[7], Liang Chang[7]

[1] State Key Laboratory of Satellite Ocean Environment Dynamics, Second Institute of Oceanography, Ministry of Natural Resources, Hangzhou 310012, China

[2] Southern Marine Science and Engineering Guangdong Laboratory (Zhuhai), Zhuhai 519080, China

[3] School of Marine Sciences, University of Maine, Orono, ME 04469, USA

[4] Virginia Institute of Marine Science, College of William & Mary Center for Coastal Resource Management, Williamsburg, VA 23185, USA

[5] Physical Oceanography Laboratory, Ocean University of China, Qingdao 266100, China

[6] Department of Atmospheric and Oceanic Sciences, Institute of Atmospheric Sciences, Fudan University, Shanghai 200438, China

[7] College of Marine Sciences, Shanghai Ocean University, Shanghai 201306, China

Received 16 October 2020; accepted 20 May 2021

Abstract

During the northeast monsoon season, Zhe-Min Coastal Current (ZMCC) travels along the Chinese mainland coast and carries fresh, cold, and eutrophic water. ZMCC is significantly important for the hydrodynamic processes and marine ecosystems along its path. Thus, this bottom-trapped plume deserves to be further discussed in terms of the major driving factor, for which different opinions exist. For this purpose, in this study, a high resolution Semi-implicit Cross-scale Hydroscience Integrated System Model (SCHISM) is established and validated. High correlation coefficients exist between along-shelf wind speeds and seasonal variations of both ZMCC volume transport and the freshwater signal. These coefficients imply that the wind is important in regulating ZMCC. However, for similar annual mean ZMCC volume transports, the extreme south boundaries of Zhe-Min Coastal Water (ZMCW) are different among different years. This difference is attracting attention and is explored in this study. According to the low wind/discharge experiment, it was found that although the volume transport of ZMCC is more sensitive to the variation of local wind speeds, the carried freshwater is limited by the Changjiang River discharge, which ultimately determines the south boundary of ZMCW. The momentum analysis at transects I and II shows that, for driving ZMCC, the along-shore wind forcing is as important as the buoyancy forcing. Note that this conclusion is supported by a zero-discharge experiment. It was also found that the buoyancy forcing varies with respect to time and space, which is due to variations of the discharge of Changjiang River. In addition, a particle tracking experiment shows that the substance carried by the Changjiang River diluted water would distribute along the Zhe-Min coastal region during the northeast monsoon season and it may escape due to the wind relaxation.

Key words: coastal current, numerical model, momentum analysis, Changjiang River diluted water, East China Sea

Citation: Zhang Yang, Chai Fei, Zhang Joseph, Ding Yang, Bao Min, Yan Yunwei, Li Hong, Yu Wei, Chang Liang. 2022. Numerical investigation of the control factors driving Zhe-Min Coastal Current. Acta Oceanologica Sinica, 41(2): 127–138, doi: 10.1007/s13131-021-1849-4

1 Introduction

The Changjiang River discharge, having a magnitude on the order of 10^4 m^3/s, carries the freshwater, sediments, nutrients, and organisms to its estuary, where its extent is important to the coastal dynamics and marine environment (Hong et al., 2011; Zhou et al., 2015; Wu and Wu, 2018). In summers and early autumns, during the southwest monsoon period, the Changjiang River diluted water usually forms a bulge, which is attached to the river mouth. This bulge is categorized as a surface-advected plume (Yankovsky and Chapman, 1997). In boreal autumns and winters when the northeast monsoon prevails, a bottom-trapped plume, which is known as Zhe-Min Coastal Current (ZMCC), usually forms and sustains.

The earliest frontal trapping theory for the bottom-trapped plume is proposed by Chapman and Lentz (1994). Evaluation of the factor that effectively drives the bottom-trapped plume, in-

Foundation item: The Scientific Research Fund of the Second Institute of Oceanography, MNR under contract Nos JG2104 and 14283; the National Natural Science Foundation of China under contract Nos 41730536, 42076010 and 42130403; the Shanghai Pujiang Program under contract No. 19PJ1404300; the Shandong Natural Science Foundation under contract No. ZR2021MD007; the Project of State Key Laboratory of Satellite Ocean Environment Dynamics, Second Institute of Oceanography, MNR under contract No. SOEDZZ2103; the Zhejiang Provincial Natural Science Foundation of China under contract No. LY21D060003.
*Corresponding author, E-mail: fchai@sio.org.cn

cluding ZMCC, has been studied in extensive research (Whitney and Garvine, 2005; Lentz and Largier, 2006; Lin et al., 2005; Zeng et al., 2012; Huang et al., 2016; Zhang et al., 2005; Wu et al., 2013; Wu and Wu, 2018; Pan et al., 2013). Whitney and Garvine (2005) proposed a wind strength index to determine if the along-shelf flow of a plume is wind-driven or buoyancy-driven. The proposed index varies with different parameters including the Kelvin number, the volume of runoff, and wind. It was indicated that the cross-shore Ekman transport is driven by the along-shore wind, which drives the along-shore geostrophic flow. Moreover, Lentz and Largier (2006), based on observations and numerical simulations, indicated that the wind force has a profound influence on the characteristics of buoyant coastal currents from rivers or estuaries.

The major driving force of ZMCC still remains controversial, while the importance of winds is mostly emphasized. Lin et al. (2005) analyzed the data of four bottom-mounted current profilers across the Taiwan Strait in winters and concluded that the subtidal current and along-shore transport generally fluctuate with the northeast winds with almost no time lag. Zeng et al. (2012) and Huang et al. (2016) used four bottom-mounted Acoustic Doppler Current Profilers (ADCPs) along a cross-shelf section in the western East China Sea to investigate the local winter circulation and its response to the wind. Analyses of Zeng et al. (2012) showed that both ZMCC and the Taiwan Warm Current (TWC) are significantly correlated with the local wind stress. Huang et al. (2016) further indicated that the correlation between winds and currents is caused by the wind-induced sea level difference, which is modified by the surface and bottom frictions. Zhang et al. (2005) pointed out that wind stresses play a key role in affecting the impacting zone of ZMCC on the diurnal timescale.

Wu et al. (2013) carried out a de-tiding measure on ZMCC along three cross-shore sections near the Zhejiang Coast and indicated that buoyancy plays an essential role in the water transport of ZMCC. Based on the momentum analysis from a numerical model, Wu and Wu (2018), focusing only on the upstream of ZMCC, further concluded that ZMCC is under the control of barotropic and baroclinic pressure gradient forces, rather than the wind stress. In addition, the southward propagating, coastally trapped Kelvin wave, which is triggered by the large-scale atmospheric fronts, is proved to be the main cause of the ZMCC variations of Pingtan (a county in the Fujian Coast), rather than the onshore/offshore water accumulation due to the local Ekman advection (Pan et al., 2013).

Observations usually focus on local or/and short-term processes (Lentz and Largier, 2006; Zeng et al., 2012; Huang et al., 2016), while numerical models take advantage of high temporal-spatial coverage and resolution. A method for studying the main factor driving the bottom-trapped plume is the sensitivity experiment. However, there are nonlinear processes between the wind effect and the buoyancy (baroclinic) force. For instance, moderate downwelling-favorable along-shore winds can tilt the front, which reduces horizontal interfaces between the buoyant water and ambient water and inhibits mixing (Fong and Geyer, 2001; Whitney and Garvine, 2005). Another method is the momentum analysis, for which it is important to discuss the scale of the current. Garvine (1995) conducted a scaling analysis of the continuity and momentum equations and, by the Kelvin number, distinguished buoyant coastal discharges with different scales. For small scale buoyant coastal discharges (K<<1), in which K is the Kelvin number, the balance in the momentum equation is between the horizontal advection and pressure gradient. At most, this balance may include up and bottom boundary stresses. However, for large scale flows (K>>1), the momentum balance is semi-geostrophic, while the along-shore balance is, at most, between the Coriolis acceleration, pressure gradient, and also up and bottom boundary stresses.

Despite numerous efforts that have been made so far, the major factor driving ZMCC remains controversial. In addition, it can be noticed that the criteria and methods of the previous works were different. For example, some works used the sea surface salinity (SSS) and sea surface temperature (SST) distributions or contour lines to define the strength of ZMCC (Zhang et al., 2005, 2020; Xu et al., 2015), while in some numerical and field studies the along-shore horizontal velocity was used (Lin et al., 2005; Zeng et al., 2012; Wu et al., 2013; Huang et al., 2016; Wu and Wu, 2018). Thus, the questions are: Do these two judgment criteria match each other? If not, do they share the same major driving factor?

To address these questions, this paper establishes a high-resolution unstructured grid numerical model and applies this model to discuss the main factors driving and sustaining ZMCC. Both the strength of ZMCC and the extent of low salinity water and their major driving factors will be discussed. The remaining text is organized as follows. In Section 2, a numerical model is described and the model-data comparison at available sites and transects is presented. In Section 3, the sensitivity experiments and momentum equation analysis will be carried out to explore the main factor driving ZMCC, and in Section 4 some conclusions will be provided.

2 Model description and validation

2.1 *Case study and model setting*

A high-resolution coastal model based on SCHISM is established in this work (Zhang et al., 2016). SCHISM is a 3D unstructured-grid model that is an upgraded version of the Semi-implicit, Eulerian-Lagrangian Finite Element (SELFE) model. SCHISM applies finite-element methods to the momentum equations and improves the advection scheme. Thus, this model is able to handle a wide range of the Courant number and avoids grid quality issues associated with the C grid. In addition, the SCHISM model employs localized sigma coordinates with shaved cells (LSC^2) and avoids the stair-stepped nature of z-levels (Zhang et al., 2016).

The main extent of ZMCC covers the coastal region of Shanghai, Zhejiang Province, and Fujian Province with a depth of less than 50 m (Xu et al., 2015). In order to locate this area in the core region of the mesh grid and to keep some distance with the open boundaries, the east and south boundaries are set to 16°51′N and 132°05′E, respectively. The bathymetry is from General Bathymetric Chart of the Oceans (GEBCO) 30 arc-sec data, as shown in Fig. 1a. In the coastal region, the horizontal resolution of the mesh grid is ~1 km, while at the deep sea it is ~7 km, as shown in Fig. 1b. Upper than 100 m, there are 20 S/σ-layers, while lower than 100 m there are 26 Z-layers, which are in total 46 layers.

At the seaside, the open boundary is divided into three parts by Philippines and Japan. The subtidal information at these boundaries is from Hybrid Coordinate Ocean Model and Navy Coupled Ocean Data Assimilation (HYCOM+NCODA) global (1/12)° analysis/reanalysis. The tidal information, including tidal amplitude, phase, and tidal current, is from the latest version of the Finite Element Solution (FES2014) tide model (Carrere et al., 2015), including eight tidal components, i.e., M_2, S_2, N_2, K_2, K_1, P_1, O_1, and Q_1. At the land side, three major rivers, the Changjiang River, Qiantang River, and Minjiang River, along ZMCC are set to be open boundaries. The hourly river discharge data of the

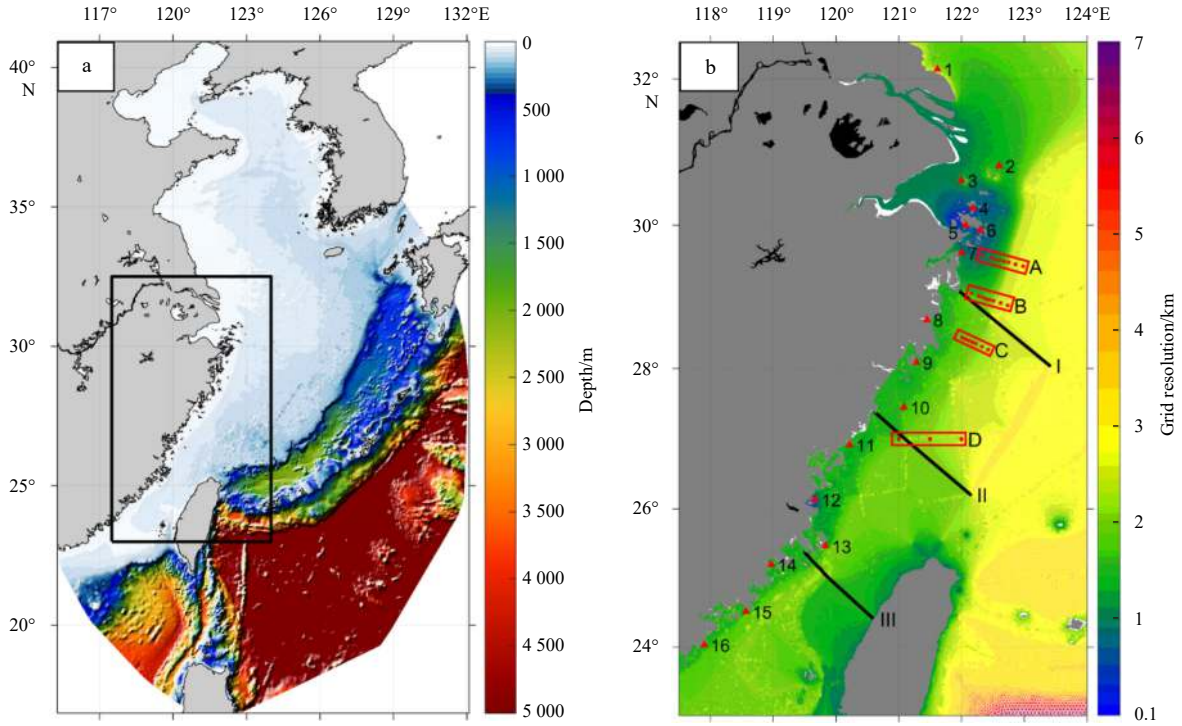

Fig. 1. The depth within the model region (a), and the mesh grid and grid resolution of the core region of the model (b) (magnifying black rectangle part of graph a). Tidal gauges were marked by red triangles. Four cruising survey transects are shown by red dots, while three cross-shore transects named I, II, and III are marked by black lines.

Changjiang River at Datong Station is from a website (http://61.191.22.157/TYFW/InfoQuery/HeDaosec.aspx) and for the other two rivers, monthly river discharge data are from *River and Sediment Bulletin of China*. The salinity of river discharge is set to zero while the temperature is from the Advanced Very High-Resolution Radiometer (AVHRR) remote sensing sea surface temperature (ftp://eclipse.ncdc.noaa.gov/pub/OI-daily-v2/NetCDF/).

The model integration period is from January 1, 2012 to December 31, 2016, with the time step being 120 s. Also, a hot-start model is used, which needs variables taken from HYCOM+NCODA global (1/12)° analysis/reanalysis. The atmosphere forcing, except 10 m winds, is from ERA5 hourly data, while winds are from the Cross-Calibrated Multi-Platform wind vector analysis (CCMP V2.0).

Harmonic tide data from tidal gauge stations along the coastal line of the core region are used for the model validation (Fig. 1). Eight data series are taken from Wu et al. (2011) and the rest are taken from the Tidal Chart of National Marine Data Information Center. The shipboard conductivity temperature depth (CTD) data to compare the model and observation results are from the open voyage of National Natural Science Foundation of China (NSFC), of which Transects A–C were observed during May 2016 and Section D was observed during February 2013 and 2014 (Fig. 1). The JPL V4.2 SMAP sea surface salinity (SSS) data are used for SSS comparison in the core region (Fore et al., 2016).

In Section 3.2, two sensitivity experiments are carried out by 20% decreasing the Changjiang River discharge and wind speeds. In Section 3.3, a zero-discharge (all three rivers) sensitivity experiment is conducted. Except for these changes, all the other setups of the sensitivity experiments, i.e., the atmosphere forcing, initial condition, and parameters, are consistent with the control run.

In Section 3.4, a particle tracking experiment is provided to give the major destinies of the material released by the Changjiang River in the Zhe-Min coastal area in the northeast monsoon seasons. The particles are released every 24 h at 0 o'clock since August 1, 2012, at a depth of 2 m, from 31.3°N and 122.3°E. The particles are kept floating at 2 m depth according to the horizontal currents for 30 days.

2.2 *The model validation*

2.2.1 *Validation of harmonic tide and volume transport*

The comparisons of the amplitude and phase of the four main tidal components are listed in Tables 1 and 2. The ratio is the magnitude of amplitude differences to the magnitude of the observation data. The mean amplitude ratios for M_2, S_2, O_1, and K_1 are 11.34%, 20.96%, 16.73%, and 11.18%, respectively. For the major constituent, the M_2 amplitudes are overestimated in the Hangzhou Bay (#2–4) and the southern region of Taiwan Strait (#14–16). However, at the other stations, the M_2 amplitudes are underestimated. For S_2, the amplitude at most stations is underestimated by the model except for the southern most of two stations. The O_1 and S_1 are relatively minor constituents in the core region. The model underestimates the O_1 amplitude at most stations, while it overestimates the K_1 amplitudes. The mean phase differences of M_2, S_2, O_1, and K_1 are 17.23%, 17.82%, 9.96%, and 17.53%, respectively. The amplitudes and phase differences at all 16 stations are within the same range of the previous works (Xu et al., 2010; Wu et al., 2011).

The simulated winter (Dec.–Feb.) volume transport across the Taiwan Strait is important because it can evaluate the model ability to reproduce the winter current in the core region. From 2012–2015, the winter volume transport across the Taiwan Strait are 0.08 Sv (1 Sv=10^6 m^3/s), 0.17 Sv, 0.48 Sv, and 0.04 Sv, respectively, with the mean value of 0.19 Sv. These values are within the

Table 1. The comparison of model results and observations of amplitudes (m) of the four major tide constituents

Num.	Station	M_2				S_2				O_1				K_1			
		OBS	SIM	DIF	RATIO	OBS	SIM	DIF	RATIO	OBS	SIM	DIF	RATIO	OBS	SIM	DIF	RATIO
1	Lüsi	1.61	1.59	0.02↓	0.97%	0.97	0.74	0.23↓	24.05%	0.10	0.13	0.03↑	28.97%	0.12	0.15	0.03↑	27.70%
2	Lühuashan	1.13	1.21	0.08↑	6.83%	0.74	0.50	0.24↓	32.50%	0.23	0.20	0.03↓	13.91%	0.31	0.31	0.00	1.01%
3	Tanhu	1.43	1.53	0.10↑	6.90%	0.85	0.53	0.32↓	37.38%	0.21	0.17	0.04↓	18.55%	0.24	0.28	0.04↑	17.98%
4	Daishan	0.91	1.00	0.09↑	10.33%	0.50	0.33	0.17↓	33.55%	0.21	0.17	0.04↓	19.19%	0.25	0.29	0.04↑	15.75%
5	Dinghai	0.85	1.05	0.20↑	23.59%	0.46	0.36	0.10↓	20.90%	0.21	0.18	0.03↓	14.46%	0.25	0.29	0.04↑	15.12%
6	Shenjiamen	1.12	1.03	0.09↓	8.25%	0.62	0.40	0.22↓	34.95%	0.23	0.18	0.05↓	21.54%	0.26	0.33	0.07↑	26.69%
7	Xize	1.36	1.15	0.21↓	15.07%	0.83	0.68	0.15↓	18.41%	0.23	0.18	0.05↓	20.22%	0.28	0.33	0.05↑	18.48%
8	Haimen	1.56	1.55	0.01↓	0.77%	0.91	0.62	0.29↓	32.06%	0.18	0.20	0.02↑	11.95%	0.30	0.32	0.02↑	5.74%
9	Kanmen	1.87	1.48	0.38↓	20.56%	0.69	0.56	0.13↓	18.59%	0.24	0.18	0.07↓	27.43%	0.33	0.29	0.04↓	11.29%
10	Nanlushan	1.77	1.28	0.49↓	27.45%	0.62	0.48	0.14↓	23.30%	0.22	0.19	0.02↓	10.44%	0.29	0.31	0.01↑	4.73%
11	Sansha	2.03	1.60	0.44↓	21.44%	0.68	0.53	0.16↓	22.85%	0.26	0.20	0.05↓	20.68%	0.32	0.32	0.00	0.77%
12	Minjiangkou	2.00	1.88	0.13↓	6.34%	0.60	0.58	0.02↓	3.67%	0.21	0.21	0.00	0.10%	0.29	0.33	0.04↑	14.89%
13	Pingtan	2.05	1.83	0.22↓	10.82%	0.62	0.54	0.08↓	13.23%	0.26	0.21	0.05↓	17.89%	0.31	0.32	0.01↑	3.56%
14	Xiuyu	2.36	2.45	0.09↑	3.70%	0.69	0.69	0.01↓	1.27%	0.26	0.23	0.03↓	11.65%	0.33	0.32	0.00	1.50%
15	Weitou	1.77	1.94	0.17↑	9.58%	0.55	0.56	0.01↑	2.07%	0.27	0.23	0.03↓	12.68%	0.32	0.34	0.02↑	5.20%
16	Jiangjunao	1.35	1.46	0.12↑	8.78%	0.36	0.42	0.06↑	16.60%	0.27	0.22	0.05↓	17.94%	0.36	0.33	0.03↓	8.50%

Note: Up arrow (↑) means overestimation while down arrow (↓) means underestimation. DIF is the absolute value of the difference between observation (OBS) and simulation (SIM) results. RATIO is DIF over OBS.

Table 2. The comparison of model results and observations of phases (°) of the four major tide constituents

Num.	Station	M_2			S_2			O_1			K_1		
		OBS	SIM	DIF	OBS	SIM	DIF	OBS	SIM	DIF	OBS	SIM	DIF
1	Lüsi	350.00	342.90	7.10	43.00	45.07	2.07	103.00	75.51	27.49	151.00	166.27	15.27
2	Lühuashan	284.00	285.63	1.63	332.00	338.69	6.69	155.00	144.67	10.33	202.00	212.70	10.70
3	Tanhu	349.00	329.18	19.82	51.00	26.12	24.88	181.00	158.65	22.35	237.00	228.91	8.09
4	Daishan	293.00	320.57	27.57	348.00	10.65	22.65	173.00	162.66	10.34	219.00	232.21	13.21
5	Dinghai	287.00	306.25	19.25	344.00	351.84	7.84	175.00	163.29	11.71	219.00	232.95	13.95
6	Shenjiamen	267.00	281.04	14.04	320.00	325.77	5.77	162.00	161.23	0.77	225.00	230.28	5.28
7	Xize	264.00	271.00	7.00	318.00	317.82	0.18	171.00	163.71	7.29	227.00	232.77	5.77
8	Haimen	270.00	263.92	6.08	330.00	315.12	14.88	197.00	183.91	13.09	243.00	248.45	5.45
9	Kanmen	251.26	269.36	18.10	292.93	316.75	23.82	178.36	192.85	14.49	217.81	250.68	32.87
10	Nanlushan	261.92	269.97	8.05	303.63	310.77	7.15	181.11	182.31	1.20	223.11	248.01	24.90
11	Sansha	280.67	299.05	18.39	322.47	340.82	18.34	197.49	195.49	2.00	234.84	256.03	21.19
12	Minjiangkou	308.62	321.92	13.30	353.99	6.06	12.06	203.29	204.89	1.61	244.27	265.80	21.53
13	Pingtan	310.50	334.89	24.39	355.73	22.15	26.42	215.54	210.67	4.87	252.83	273.80	20.98
14	Xiuyu	332.82	16.38	43.56	21.06	76.16	55.10	226.83	250.89	24.06	268.32	306.61	38.29
15	Weitou	341.46	4.70	23.24	29.52	60.96	31.45	231.39	237.53	6.14	278.18	299.99	21.82
16	Jiangjunao	353.23	17.42	24.19	50.26	76.12	25.86	239.04	237.41	1.64	284.20	305.35	21.16

Note: DIF is the absolute value of the difference between OBS and SIM. RATIO is DIF over OBS.

range of (0.12 ± 0.33) Sv, which was observed by Lin et al. (2005). Comparing to over 1.0 Sv volume in the other seasons, when TWC prevails, this range shows a balance between TWC and ZMCC.

2.2.2 *Validation of the sea surface salinity*

The JPL V4.2 SMAP monthly averaged SSS data are available since April 2015. Since then, the model-JPL SSS comparisons are carried out for the next year. Although SWAP includes the land correction and enhances spatial resolution (Fore et al., 2016), the SSS data for very close areas to the coast is still unavailable (Fig. 2). Based on former works, 32 is set as the outer line of Zhe-Min Coastal Water (ZMCW) (Xu et al., 2015), thus, Fig. 2 only shows SSS lower than 32. The seasonal cycles of the ZMCW coverage are visible from both the JPL data and the model results. From April to August 2015, ZMCW retreat from the Taiwan Strait and gradually formed a bulge at the Changjiang River Estuary. The SSS pattern of the JPL data is quite similar to the model results. Both JPL and model results show that ZMCW started to spread along the Zhe-Min Coast since September 2015 and reached its maximum coverage in February 2016. The main part of the low salinity water attached to the Chinese mainland coast is matching between the JPL data and model results, except for the much lower SSS extent of the JPL data in the Taiwan Strait. Xu et al. (2015) analyzed over 700 CTD profiles within this core region and determined the eastern boundary of ZMCW in winter, defined by SSS of 32. In the Taiwan Strait, the eastern boundary is no farther than 58.2 km from the Chinese mainland coast. The low salinity water showed by the JPL data is very likely unreliable. The outer line of the model results in winter is reasonable according to Fig. 7 and Table 1 of Xu et al. (2015).

2.2.3 *Validation of cruising survey data*

To examine the model performance at the Zhe-Min coastal region, both observed temperature and salinity along Transects

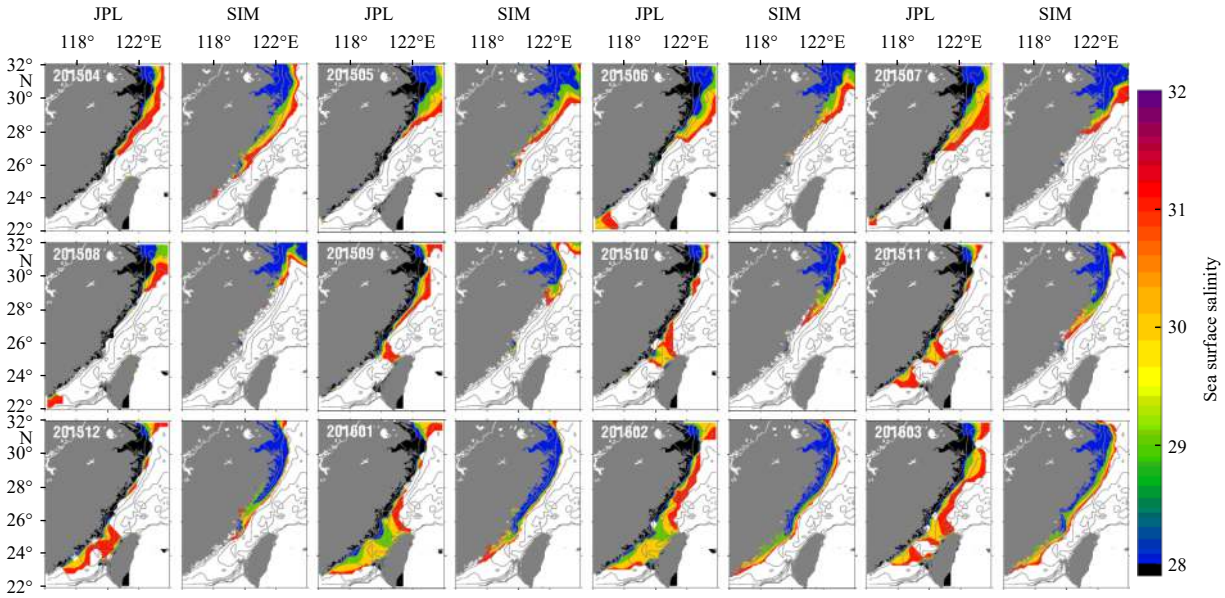

Fig. 2. Comparison of sea surface salinity in the core region between JPL V4.2 SMAP monthly averaged data and simulation results, from April 2015 to March 2016. The coastal region with no JPL data is black.

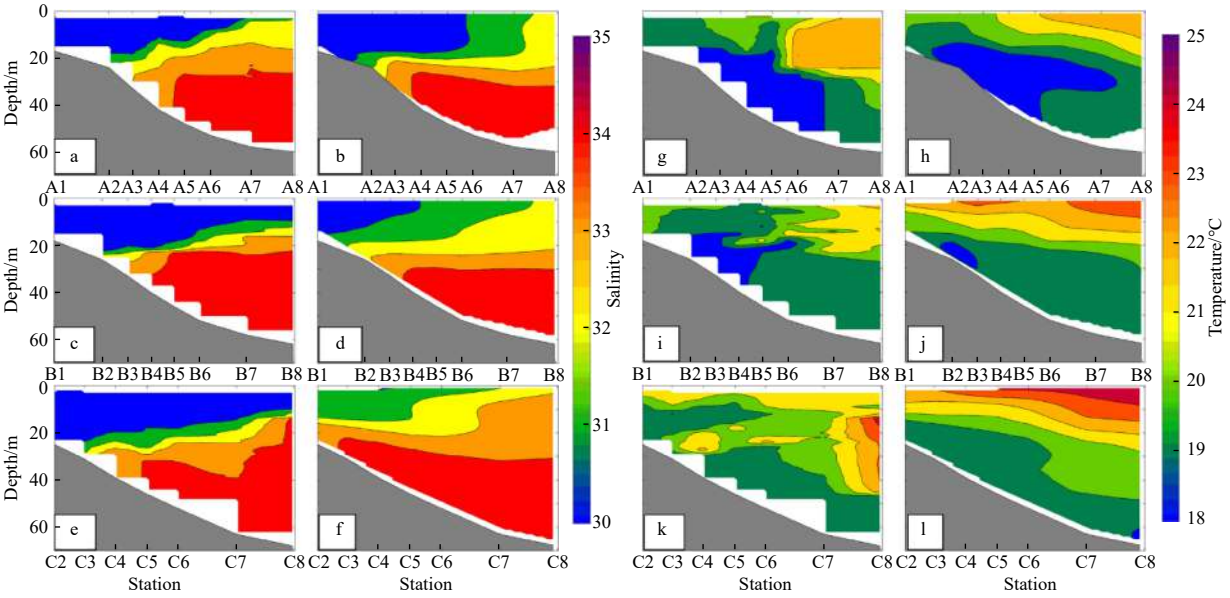

Fig. 3. Comparison of the salinity (left 6 panels), and the temperature (right 6 panels) distributions along Transects A–C. The first and third columns are for the observation data, while the second and forth columns are for the simulation results.

A–D are compared to the model results. Figure 3 shows both the observed temperature-salinity (*T*-*S*) distribution along transects A–C and the time-matched model results in May 2016. The main *T*-*S* structure is properly captured by the model although some details may differ. Both simulation results and observation data show the pattern of the surface-advected plume. Because of relatively weak wind stress in late spring, the water was not well mixed from bottom to top. Thus, both the salinity and temperature show an obvious stratification.

For the salinity, the best match is at the Transect A. The Transects B and C well reproduce the structure, which is the low salinity at the top and coastal side. However, the surface salinity is overestimated by 1–2, especially at the Transect C. The best match for the temperature also happens at the Transect A. At the Transect B, the cold bottom water near the Station C4 is reproduced, while the surface temperature is overestimated by 1–2℃. For the Transect C, the warm water (24℃) was observed at depths of 15–45 m at the Station C8, while the model results are more stratified and the warm water lies at the top.

The *T*-*S* data at the Transect D was obtained in February of 2013 and 2014 when ZMCM occupied the coastal region. This is during the ZMCC prevail season when the bottom trapped feature is clearly captured by the model and observations. Comparing to the Transects A–C, the water is better mixed due to the strong northeast monsoon (Fig. 4). The red contour line in Figs 4a–d is the outline of ZMCW denoted by 32. Both observed data and model results show that the east boundary of the ZMCC water is not far away from 121°E. Comparing to the observed data, the sa-

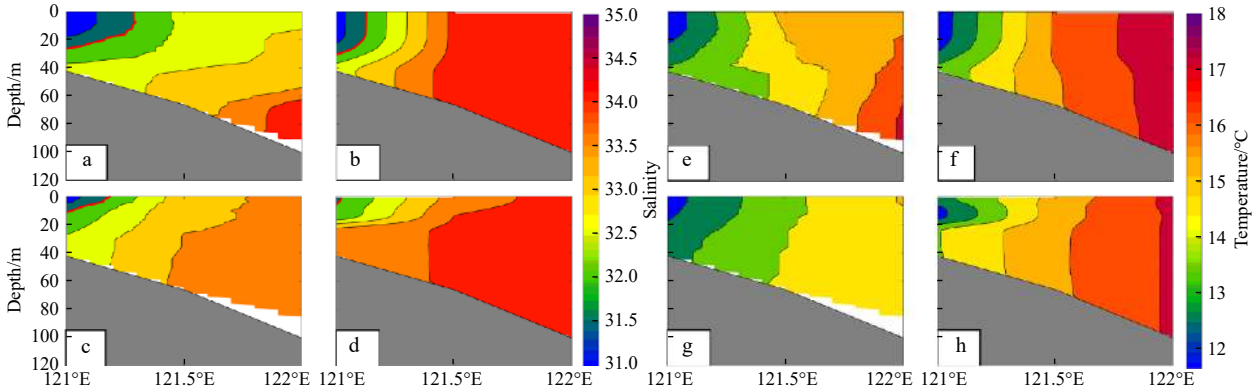

Fig. 4. Comparison of the salinity (left 4 panels) and the temperature (right 4 panels) distributions along Transect D, for the month of February 2013 (up 4 panels) and February 2014 (bottom 4 panels). The first and third columns are for the observation data, while the second and forth columns are for the simulation results.

linity at the offshore side is overestimated by 0.5–1. For the temperature, the model also well reproduces the low-temperature water at the coastal side and the stratification of this transect. However, the temperature at the offshore side is overestimated by ~1℃. Figures 4a and c show that the thickness of ZMCW at 121°E is much thicker in February 2013 than in February 2014. After the horizontal interpolation, the east boundary of ZMCW is farther from the coast in February 2013 than in February 2014. The model results also show the similar annual difference, as can be seen in Figs 4b and d.

3 Results

3.1 *Seasonal variation of ZMCC*

In order to fully describe the seasonal variation of ZMCC and its regional difference, the model results at three cross-shelf transects (Transects I–III) along the coastal region are extracted for analysis. The volume transport of ZMCC (VT_{ZMCC}) at each transect is calculated as:

$$VT_{\mathrm{ZMCC}} = \int_{V<0} V \mathrm{d}A, \tag{1}$$

where V and A are the current velocity normal to the cross-shelf transect and the area of each element of the "ZMCC transect", respectively. The element of "ZMCC transect" is defined by two conditions: (1) the southwestward current is the direction at the element and (2) 60% of the 100 ambient element's current must be in the southwestward direction.

A freshwater index (FWI) is calculated as:

$$\mathrm{FWI} = \frac{\int_{V<0} FV \mathrm{d}A}{VT_{\mathrm{ZMCC}}}, \tag{2}$$

where $F = s_0 - sal$, and sal is the salinity of each element of "ZMCC transect". Following a previous work (Xu et al., 2015), in the present study, 32 is used to define the boundary of ZMCW. Thus s_0 is set to 32 in order to describe the proportion of Changjiang River diluted water that ZMCC carries. Figure 5a shows the mean Changjiang River discharge and monthly mean projected wind speeds in the core region. The projected direction is 36° west of the south, which is the approximate direction of the core region's coastal line. In Figs 5b–d, the solid lines show the monthly mean VT_{ZMCC} and FWI for the four northeast monsoon periods.

Both projected wind speeds and Changjiang River discharge show a clear seasonal variation, as can be seen in Fig. 5a. The Changjiang River discharge reaches its peak in June or July and its minimum value in January. The projected wind is strong during autumn and winter (Sept. to the next Feb.).

In addition, both VT_{ZMCC} and FWI show seasonal variations, which for VT_{ZMCC} can be detected since every September and it is well coincident with the month that wind speed becomes positive. During the autumn and winter, the variation of monthly mean VT_{ZMCC} is highly correlated with projected wind speeds with no time lag (Table 3), for which the P value of the correlation relationship is all lower than 0.05. The mean value in each northeast monsoon season (blue numbers in each subplot) shows that VT_{ZMCC} exhibits a southward increasing trend among the three transects. The simulation results (not shown here) show that during the northeast monsoon season and due to the strong northeast winds, the Kuroshio intrusion water usually joins ZMCC along its path and thus, when ZMCC goes south, it gradually increases the volume transport.

During the autumn and winter, the variation of the monthly mean FWI is also highly correlated with projected wind speeds with 1–2 month delay (Table 4), for which the P value of the correlation relationship is all lower than 0.05. No obvious correlation relationship can be found between the Changjiang River discharge and VT_{ZMCC} or FWI. At the Transect I, FWI is detected as positive simultaneously with VT_{ZMCC} except for 2013 and 2014. At the other two transects, FWI is detected at least one month later than VT_{ZMCC}. This means that when the northeast monsoon starts, ZMCC is triggered simultaneously and it takes time to transport freshwater to the south. Note that changes of FWI among three transects are obvious. The mean FWI (red number in each subplot) becomes smaller when it goes south. Additionally, the time taken by FWI to reach its peak values has a southward delaying trend.

Overall, the seasonal variation of VT_{ZMCC} is highly correlated with projected wind speeds, without time lag. This is consistent with previous works based on observations (Zeng et al., 2012; Huang et al., 2016). This high correlation relationship can extensively cover the whole extent of ZMCC and exists during the northeast monsoon periods. The seasonal variation of FWI is also highly correlated with projected wind speeds, with 1–2 months time lag. ZMCC is triggered by the northeast monsoon as it takes time to carry Changjiang River diluted water south.

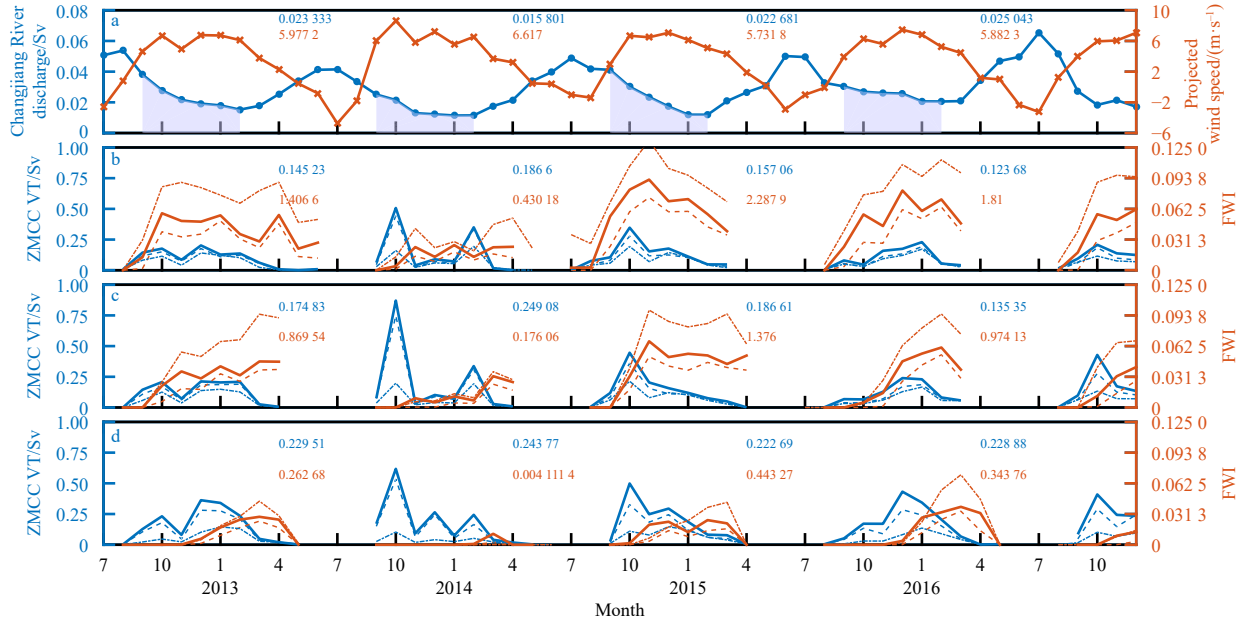

Fig. 5. The monthly mean Changjiang River discharge and projected wind speeds (a), and the Zhe-Min Coastal Current (ZMCC) volume transport (VT) and freshwater index (FWI) at Transects I (b), II (c), and III (d). In a, blue and red numbers are the mean Changjiang River discharge and projected wind speeds averaged in each northeast monsoon season (Sept. to next Feb.), respectively, 1 Sv=106 m3/s. In b–d, the solid blue lines represent VT and the solid red lines represent FWI. The blue and red numbers are the mean values of the above two parameters averaged in each northeast monsoon season (Sept. to next Feb.). The dashed lines are simulation results from the low Changjiang River discharge case. The dot-dashed lines are simulation results from the low wind speed case.

Table 3. Correlation coefficients between ZMCC volume transport and projected wind speed at 3 transects with 0–2 month lag

Transect	Delay month		
	0	1	2
I	0.850	0.449	–0.001
II	0.840	0.374	–0.117
III	0.957	0.613	0.144

Table 4. Correlation coefficients between freshwater index and projected wind speed at 3 transects with 0–4 month lag

Transect	Delay month				
	0	1	2	3	4
I	0.55	0.61	0.42	0.14	–0.16
II	0.31	0.65	0.66	0.53	0.29
III	0.07	0.43	0.52	0.50	0.40

3.2 *Annual variation of ZMCC*

Figure 6 shows the maximum monthly mean extent of ZMCW for each year. Except for March 2014, the south boundary of ZMCW reaches 23°N for each year, while in March 2014, the low salinity water (<29) is centralized in the estuary of the Changjiang River and Qiantang River. The different ZMCW thicknesses and east boundary longitude at the Transect D between 2013 and 2014 are the proof of this annual difference (Fig. 4). Note that in March 2014, the south boundary of ZMCW only reaches 25°N, corresponding to the higher level of the projected wind speed and lower level of Changjiang River discharge, shown in Fig. 5a by red and blue numbers, respectively. The mean VT_{ZMCC} at each transect of the northeast monsoon season in 2013 is higher than in the other years, with blue numbers in Figs 5b–d. However, significant low numbers of mean FWI, shown by red in Figs 5b–d, can be noticed at each transect. This means that although strong ZMCC is driven by the robust northeast wind, less freshwater is

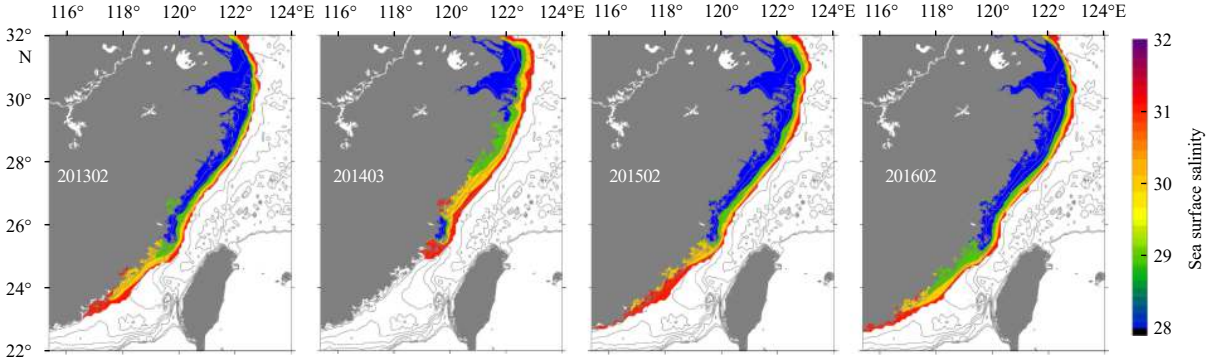

Fig. 6. The annual maximum extent of Zhe-Min coastal water illustrated by monthly mean sea surface salinity.

carried by ZMCC in the northeast monsoon season of 2013, which could be due to the lower Changjiang River discharge during this period. Note that the mean Changjiang River discharge from September 2013 to February 2014, which is shown by blue numbers in Fig. 5a, is about 66.7% of the other three years.

In order to further explore this issue, two sensitivity experiments are carried out by 20% decreasing the Changjiang River discharge and wind speeds. The results are shown by dashed and dot-dashed lines in Figs 5b–d. When the discharge is decreased by 20%, VT_{ZMCC}s are 77%, 82%, and 88% of the control run at the three transects, while FWIs are 62%, 60%, and 47% of the control run. When the wind speed is decreased by 20%, VT_{ZMCC}s are 68%, 60%, and 50% of the control run and FWIs are 168%, 158%, and 123% of the control run. When the discharge is decreased by 20%, both VT_{ZMCC} and FWI are reduced and the total freshwater transport is approximately 50% of the control run. This is because when buoyancy water input is reduced, the buoyance force driving ZMCC is decreased and the freshwater supply is reduced too. However, when the wind speed is decreased by 20%, VT_{ZMCC} is decreased significantly, while FWI is higher than that of the control run. In this case, although the wind force driving ZMCC is reduced, which is due to lower downwelling favorable winds, the width of ZMCW (defined by 32) is expanded and makes the transect of ZMCC fresher. In addition, since the source of freshwater is unchanged, the total freshwater transport is similar to the control run.

Therefore, the sensitive experiment shows that the annual variability of the ZMCC strength, denoted by mean VT_{ZMCC}, is more sensitive to the variability of projected wind speeds. Also, the freshwater transported by ZMCC is more sensitive to Changjiang River discharge. As a result, the annual maximum extent of the Changjiang River diluted water in the Zhe-Min coastal region is mainly controlled by the Changjiang River discharge itself. Note that the wind may have the opposite effect on VT_{ZMCC} and FWI, thus, it weakly modulates the maximum extent of ZMCW.

3.3 *Momentum analysis*

The momentum analysis is carried out to quantitatively describe the contribution of different momentum sources to ZMCC. The simplified momentum equation of SCHISM model is

$$\frac{\mathrm{D}u}{\mathrm{D}t} = f(v, -u) - g\nabla\eta + m_z - \frac{g}{\rho_0}\int_z^\eta \nabla\rho \mathrm{d}\zeta, \tag{3}$$

where m_z represents the vertical viscosity, and $\mathrm{D}u/\mathrm{D}t$ is the acceleration term, $f(v, -u)$ is the Coriolis term, $g\nabla\eta$ is the barotropic term, and $\frac{g}{\rho_0}\int_z^\eta \nabla\rho \mathrm{d}\zeta$ is the baroclinic term.

Before the momentum analysis, the flow scale (Kelvin number, K) of ZMCC needs to be calculated. The K represents the ratio of the across-shore length-scale (w) to the baroclinic Rossby radius (c/f) (Garvine, 1995), which is calculated as

$$K = \frac{w}{c/f}, \tag{4}$$

where c is the baroclinic gravity-wave phase speed and f is the Coriolis parameter. Chelton et al. (1998) provided the global first baroclinic Rossby radius of deformation, and according to Fig. 6 of this reference, c/f is at most 40 km in the core region. According to over 700 CTD profiles, the maximum width of ZMCC is 94.5 km and the mean value of w is 55.8 km. Thus, K is approximately larger than 1.4 for ZMCC and the momentum balance should be semi-geostrophic. The momentum balance should be between the Coriolis acceleration, cross-shore pressure gradient (including barotropic and baroclinic), and also cross-shore up and bottom boundary stresses (Garvin, 1995).

Thus, Eq. (3) could be further simplified as

$$f(v) = g\nabla\eta_x + \frac{g}{\rho_0}\int_z^\eta \nabla\rho_x \mathrm{d}\zeta - m_z, \tag{5}$$

where $f(v)$, m_z, $g\nabla\eta_x$, and $\frac{g}{\rho_0}\int_z^\eta \nabla\rho_x \mathrm{d}\zeta$ are the Coriolis term, the vertical viscosity, the barotropic, and baroclinic terms at the cross-shelf direction. A term balance of Eq. (5) is done to make sure that the following analysis is proper. The momentum balance can be achieved at Transects I and II, but it is not stable and strictly achieved at Transect III (not shown here). This is probably because of the complex bathymetry and dynamics in the Taiwan Strait, i.e. the competition between ZMCC and TWC. Thus, the momentum analysis will be done at Transect I and Transect II.

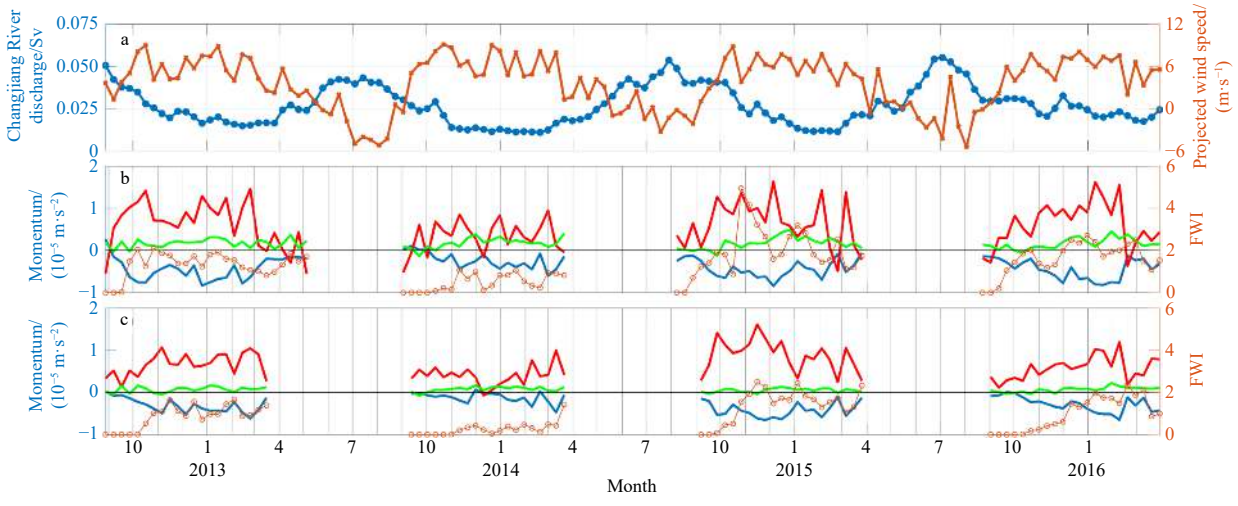

Fig. 7. The 10-days mean Changjiang River discharge and projected wind speeds (a), and the barotropic (solid red), baroclinic (solid blue), vertical viscosity (solid green) terms and freshwater index (FWI, circle) at Transect I (b), and Transect II (c) for the control run. 1 Sv=10^6 m^3/s.

As the monthly average cannot represent the high frequency dynamic processes and daily mean is too chaotic, Fig. 7a shows the 10-days averaged Changjiang River discharge and projected wind speeds. They show a similar trend to the monthly mean Changjiang River discharge and projected wind speeds, as shown in Fig. 5a, and the 10-days averaged winds show high frequency variations. Figures 7b and c show the 10-days averaged $g\nabla\eta_x$, $\frac{g}{\rho_0}\int_z^\eta \nabla\rho_x \mathrm{d}\zeta$, and m_z within the "ZMCC transect", and FWI at three transects.

The variable m_z is the direct momentum input from the wind stress and bottom friction at the offshore direction. Also, $\frac{g}{\rho_0}\int_z^\eta \nabla\rho_x \mathrm{d}\zeta$ is deduced from the onshore density gradient $(\nabla\rho_x)$ due to the Changjiang diluted water. Csanady (1978) described a frontal adjustment model, in which when a front forms, water level rises with the density reduction at the shoreside of the front. Note that the barotropic pressure gradient is seaward and the baroclinic pressure gradient is shoreward. Then, this front has a tendency to adjust geostrophically, thereby generating a surface-intensified alongshore jet (Chapman and Lentz, 1994). Thus, a positive $g\nabla\eta_x$ at the offshore direction is composed of two parts: the offshore pressure gradient due to downwelling favorable along-shore wind and the water level rise due to buoyancy water from Changjiang River discharge.

The mean values of the above three terms, calculated from September to next March during each northeast monsoon season, are shown in Table 5. According to the frontal adjustment model of Csanady (1978), it is assumed that a part of the barotropic term should be balanced with the baroclinic term. Thus, the absolute value of the baroclinic term is used to represent the buoyancy forcing, while the wind forcing is estimated by the sum of the barotropic and baroclinic terms. Note that these forces are listed in Table 5. It is noticed that, at both transects, annual differences of $g\nabla\eta_x$ and m_z are not remarkable.

Table 5 shows that the wind forcing is competitive with the buoyancy forcing. At Transect I, the buoyancy forcing is stronger and at Transect II, the wind forcing prevails. Note that the vertical viscosity plays a minor role at both transects. The baroclinic forcing shows a strong annual variability and spatial difference. Because of the low Changjiang River discharge from September 2013 to February 2014, $\frac{g}{\rho_0}\int_z^\eta \nabla\rho_x \mathrm{d}\zeta$ is much lower in this period than in the other three years. As less freshwater is transported to the south, when ZMCC goes to the south, $\frac{g}{\rho_0}\int_z^\eta \nabla\rho_x \mathrm{d}\zeta$ gets lower. Also, because of the low Changjiang River discharge from September 2013 to February 2014, during this period the wind forcing is the major driving forcing of ZMCC.

In order to further explore the role of Changjiang River discharge in modulating ZMCC, a zero-discharge model experiment is carried out. The momentum analysis is shown in Fig. 8. When freshwater input from discharge is closed, ZMCC is still active in winter, but much weaker than that of the control run. The southwestward current could not be detected occasionally, as shown in Figs 8b and c. The speed and width of ZMCC are smaller than those in the control run (figures not shown here). For the zero-discharge run, the barotropic term is more important than the other two terms for all three transects. However, the mean value of the barotropic term is about half of that of the con-

Table 5. The mean barotropic, baroclinic, and vertical viscosity terms and the sum of barotropic and baroclinic terms at Transect I and Transect II, calculated from September to next March, and the total mean value

Terms	Transect	2012	2013	2014	2015	Mean
Barotropic/(m·s^{-2})	I	6.11×10^{-6}	4.96×10^{-6}	6.42×10^{-6}	6.29×10^{-6}	5.94×10^{-6}
	II	6.64×10^{-6}	6.14×10^{-6}	8.72×10^{-6}	5.75×10^{-6}	6.81×10^{-6}
Baroclinic/(m·s^{-2})	I	-4.30×10^{-6}	-2.35×10^{-6}	-4.28×10^{-6}	-4.43×10^{-6}	-3.84×10^{-6}
	II	-3.10×10^{-6}	-1.24×10^{-6}	-4.20×10^{-6}	-2.82×10^{-6}	-2.84×10^{-6}
Vertical viscosity/(m·s^{-2})	I	1.72×10^{-6}	1.72×10^{-6}	1.65×10^{-6}	1.63×10^{-6}	1.68×10^{-6}
	II	6.86×10^{-7}	7.67×10^{-6}	4.98×10^{-6}	6.68×10^{-7}	6.55×10^{-7}
Barotropic+Baroclinic/(m·s^{-2})	I	1.81×10^{-6}	2.60×10^{-6}	2.14×10^{-6}	1.86×10^{-6}	2.10×10^{-6}
	II	3.54×10^{-6}	4.90×10^{-6}	4.53×10^{-6}	2.92×10^{-6}	3.97×10^{-6}

Fig. 8. The 10-days mean Changjiang River discharge and projected wind speeds (a), and the barotropic (solid red), baroclinic (solid blue), vertical viscosity (solid green) terms and freshwater index (FWI, circle) at Transect I (b) and Transect II (c) for no-discharge run.

trol run. Note that this fact confirms the equally important role of wind forcing and buoyancy forcing in driving ZMCC. Closing the freshwater input may significantly change the feature of the bottom-trapped bloom and may weaken its strength, which further changes the impact of the wind stress. Note that the quantitative analysis is complex and may be discussed in a separated work.

To sum up, the along-shore wind plays as important role as the buoyancy water does in driving ZMCC. Also, during dry year of the Changjiang River, the baroclinic forcing is relatively weaker than the wind forcing. The buoyancy forcing can significantly modulate the winds' contribution to ZMCC and, in the meantime, it can directly modulate ZMCC. Note that the zero-discharge experiment carried out in this study shows that ZMCC is significantly weakened when the Changjiang River discharge is close. However, the wind stress and buoyancy are interactively modulating ZMCC and if either of them shuts down, the structure of ZMCC may dramatically be affected.

3.4 *Substance transport during the northeast monsoon season*

A particle tracking experiment is carried out to analyze the whereabouts of the floating substance, which the Changjiang River diluted water carries. The configurations of this experiment are given in Section 2.

Figure 9 shows the start point (green triangle), the track (red lines), and the final position (squares). The black and gray vectors are the mean winds in the first and second halves of the month. The color of the squares is black for the 1st day released particle in every month and gradually turns to white for the last day released particle.

From the late half of August (low gray level squares in August), most particles end up in the coastal region in the south of Changjiang River Estuary. This is because in the second half of August winds gradually turn to the south-west direction (gray vectors) and in September the wind speed is relatively low and the wind directions are mostly in favor of ZMCC.

The moment, when most particles turn around and escape from ZMCC, varies for different years. In 2013 and 2014, particles start to change direction in the late half of February (white squares). In 2015 and 2016, this moment is about one month earlier, which is mainly because of the early loss of favorable winds to ZMCC (black vectors in February of 2015 and 2016) comparing to those in 2013 and 2014.

During other months in the northeast monsoon season, particles basically drift in the southwest direction along the coast, except for several collective direction changes (November 2013, and December 2014) during the northeast monsoon wind relaxation. In 2012, 2014, and 2015, after 30 days of drifting, the final position of some particles can be lower than 25°N, while in 2013, the most south destination is about 26°N.

If one looks at the tracks of the particles, which change direction and escape from ZMCC, regardless of whether during the winter-time monsoon winds or after, it can be noticed that the offshore shifting is always accompanied by the direction change, which corresponds well with the front tilting theory for the coastal front during the downwelling favorable season (Lentz and Largier, 2006). During downwelling winds, the onshore Ekman transport causes the plume front to steepen, while for upwelling winds or relaxation of downwelling winds, the plume front becomes flat and pushes the surface water offshore. This experiment shows that the substance carried by ZMCC may escape during the northeast monsoon wind relaxation event. However, most substances distribute along the Zhe-Min coastal region.

Since 2000, the location and scale of the spring phytoplankton bloom in the Zhe-Min coastal area have been varying (Hong et al., 2011; personal contact with Caiyun Zhang from Xiamen University). This particle tracking experiment aims to provide a quick look at the distribution of the substance carried by Changjiang River diluted water when ZMCC prevails. This may provide information for the pelagic ecosystem research in the Zhe-Min coastal area.

4 Conclusions

It is known that the previous studies analyzed different criteria and methods, including the distributions of variables at sea surface (SSS and SST) and the velocity of the along-shore currents, to define the strength of ZMCC. Additionally, the major factor driving ZMCC is still under question. Thus, this study attempts to find if these judgment criteria match each other and if they share the same major driving factor. Therefore, a ZMCC model case was established based on SCHISM. The amplitude and phase of four major tidal constituents at 16 coastal stations were well reproduced by the model with acceptable accuracy. It was found that the winter volume transport through the Taiwan Strait during the integration period corresponds well with historical observations. Both monthly mean SSS and instantaneous *T*-*S* profiles were well validated by remote sensing data and cruising survey data. Therefore, it is proved that the model is appropriate for the ZMCC analysis. VT_{ZMCC} and FWI of the "ZMCC transect" were calculated to evaluate the strength of ZMCC and the taken freshwater. It is no surprise that the seasonal variation of the above two variables is highly correlated with projected wind speeds. Although for the strength of ZMCC there is no time lag, there is 1–2 months delay for the information of freshwater.

Furthermore, according to the sensitive experiment, it was found that the annual variation of ZMCC, defined by its volume transport, is more sensitive to the variation of projected wind speeds, while the Changjiang River discharge can modulate the strength of ZMCC.

The momentum analysis provided a more comprehensive and clear view about contributions of the wind and buoyancy forces. ZMCC is categorized as a large-scale plume as its Kelvin number is larger than one. Additionally, according to the term balance analysis of the momentum equation, the momentum balance is semi-geostrophic at Transects I and II. At these two transects, it was found that the wind-induced sea level difference, and buoyancy water from Changjiang River discharge are two major driving terms and they play equally important roles in driving ZMCC. This conclusion is also supported by a zero-discharge experiment.

To address the two judgment criteria of the strength of ZMCC, presented in Section 1, the sensitivity experiment shows that the Changjiang River discharge is the major factor for controlling the freshwater carried by ZMCC and for controlling the freshwater extent in the Zhe-Min coastal region during the northeast monsoon season. The along-shore horizontal velocity or VT_{ZMCC} is controlled jointly by the alongshore wind velocity and buoyancy water from Changjiang River discharge. Note that the freshwater transport and extent of ZMCW are more sensitive to Changjiang River discharge. Thus, comparing with VT_{ZMCC}, the ZMCC strength defined by velocity/volume transport and horizontal salinity/temperature contour may mismatch when the Changjiang River discharge varies.

Particle tracking experiments were also deployed to check the distribution of the substance from the Changjiang River discharge when ZMCC prevails. The results showed that most particles drift along with ZMCC and distribute in the Zhe-Min

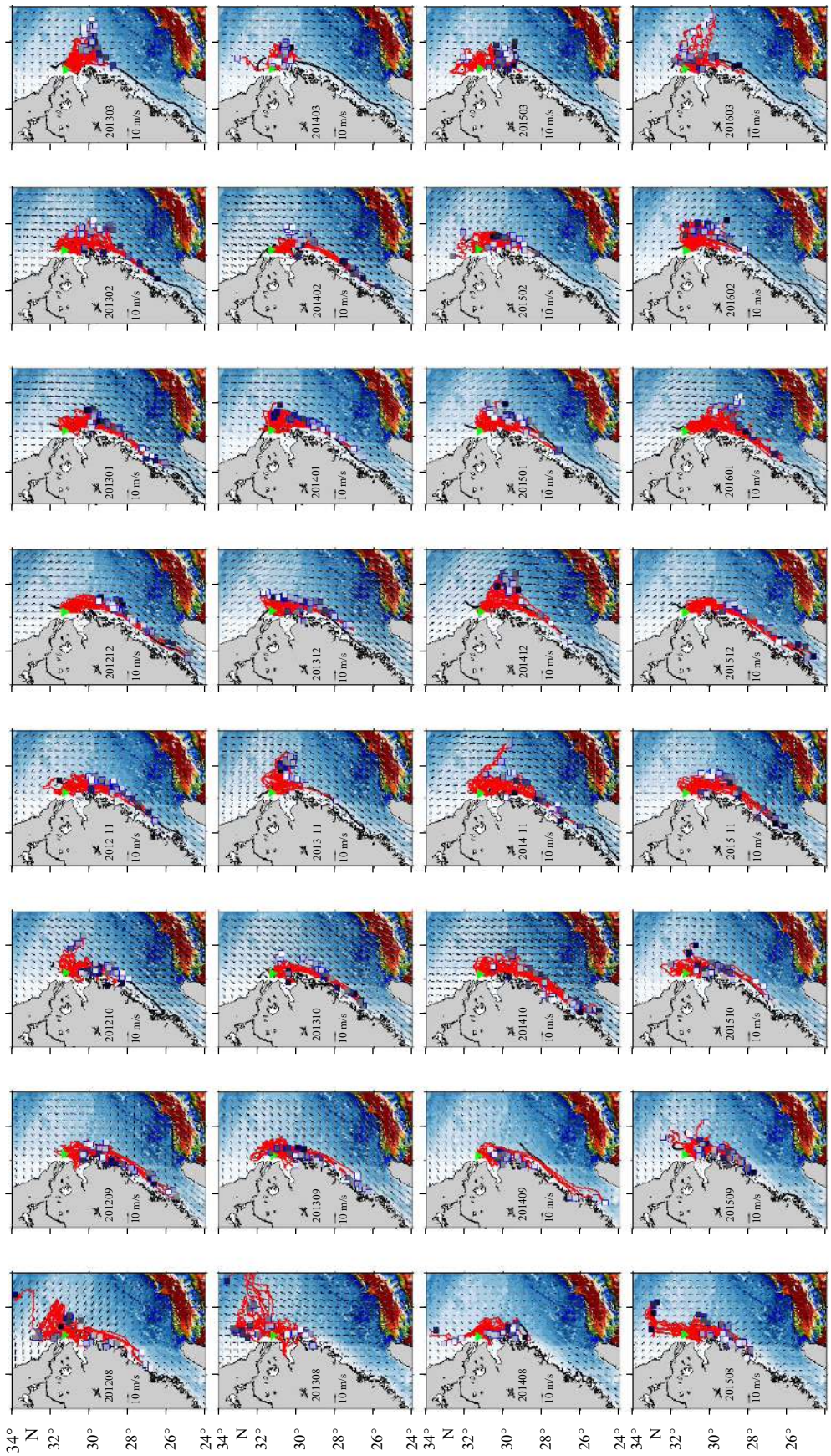

Fig. 9. The drifting trajectory (red lines) of particles released at 31.3°N and 122.3°E (green triangle), and their location (squares) after 30 days. The black and gray vectors represent the mean winds in the first and second halves of the month. In each month, the marker face color is black for the 1st day and gradually turns to white for the last day. The black lines are the 32 contour lines indicating the extent of Zhe-Min Coastal Current.

coastal region. In addition, the winter-time wind relaxation events may let particles escape from ZMCC and drift toward the northeast.

Acknowledgements

We gratefully acknowledge the invaluable contribution of Weibing Guan, Jiliang Xuan, Wenzhou Zhang, Haiqing Yu, Emil V. Stanev, Johannes Pein and Benjamin Jacob. This work was improved because of precious comments from three anonymous reviewers, and we are so grateful.

References

Carrere L, Lyard F, Cancet M, et al. 2015. FES 2014, a new tidal model on the global ocean with enhanced accuracy in shallow seas and in the Arctic region. In: EGU General Assembly Conference. Vienna, Austria: EGU

Chapman D C, Lentz S J. 1994. Trapping of a coastal density front by the bottom boundary layer. Journal of Physical Oceanography, 24(7): 1464–1479, doi: 10.1175/1520-0485(1994)024<1464:TOACDF>2.0.CO;2

Chelton D B, DeSzoeke R A, Schlax M G, et al. 1998. Geographical variability of the first baroclinic Rossby radius of deformation. Journal of Physical Oceanography, 28(3): 433–460, doi: 10.1175/1520-0485(1998)028<0433:GVOTFB>2.0.CO;2

Csanady G T. 1978. Wind effects on surface to bottom fronts. Journal of Geophysical Research: Oceans, 83(C9): 4633–4640, doi: 10.1029/JC083iC09p04633

Fong D A, Geyer W R. 2001. Response of a river plume during an upwelling favorable wind event. Journal of Geophysical Research: Oceans, 106(C1): 1067–1084, doi: 10.1029/2000JC900134

Fore A G, Yueh S H, Tang Wenqing, et al. 2016. Combined active/passive retrievals of ocean vector wind and sea surface salinity with SMAP. IEEE Transactions on Geoscience and Remote Sensing, 54(12): 7396–7404, doi: 10.1109/TGRS.2016.2601486

Garvine R W. 1995. A dynamical system for classifying buoyant coastal discharges. Continental Shelf Research, 15(13): 1585–1596, doi: 10.1016/0278-4343(94)00065-U

Hong Huasheng, Chai Fei, Zhang Caiyun, et al. 2011. An overview of physical and biogeochemical processes and ecosystem dynamics in the Taiwan Strait. Continental Shelf Research, 31(6): S3–S12, doi: 10.1016/j.csr.2011.02.002

Huang Daji, Zeng Dingyong, Ni Xiaobo, et al. 2016. Alongshore and cross-shore circulations and their response to winter monsoon in the western East China Sea. Deep-Sea Research Part II: Topical Studies in Oceanography, 124: 6–18, doi: 10.1016/j.dsr2.2015.01.001

Lentz S J, Largier J. 2006. The influence of wind forcing on the chesapeake bay buoyant coastal current. Journal of Physical Oceanography, 36(7): 1305–1316, doi: 10.1175/JPO2909.1

Lin S F, Tang T Y, Jan S, et al. 2005. Taiwan Strait current in winter. Continental Shelf Research, 25(9): 1023–1042, doi: 10.1016/j.csr.2004.12.008

Pan Aijun, Wan Xiaofang, Guo Xiaogang, et al. 2013. Responses of the Zhe-Min Coastal Current adjacent to Pingtan Island to the wintertime monsoon relaxation in 2006 and its mechanism. Science China Earth Sciences, 56(3): 386–396, doi: 10.1007/s11430-012-4429-9

Whitney M M, Garvine W R. 2005. Wind influence on a coastal buoyant outflow. Journal of Geophysical Research: Oceans, 110(C3): C03014

Wu Hui, Deng Bing, Yuan Rui, et al. 2013. Detiding measurement on transport of the Changjiang-derived buoyant coastal current. Journal of Physical Oceanography, 43(11): 2388–2399, doi: 10.1175/JPO-D-12-0158.1

Wu Tianning, Wu Hui. 2018. Tidal mixing sustains a bottom-trapped river plume and buoyant coastal current on an energetic continental shelf. Journal of Geophysical Research: Oceans, 123(11): 8026–8051, doi: 10.1029/2018JC014105

Wu Hui, Zhu Jianrong, Shen Jian, et al. 2011. Tidal modulation on the Changjiang River plume in summer. Journal of Geophysical Research: Oceans, 116(C8): C08017, doi: 10.1029/2011JC007209

Xu Jindian, Huang Jiang, Qiu Yun, et al. 2015. Spatial structure characteristics of Zhejiang and Fujian coastal water and their evolution. Journal of Tropical Oceanography, 34(1): 1–7

Xu Hongzhou, Zhang Keqi, Shen Jian, et al. 2010. Storm surge simulation along the U. S. east and gulf coasts using a multi-scale numerical model approach. Ocean Dynamics, 60(6): 1597–1619, doi: 10.1007/s10236-010-0321-3

Yankovsky A E, Chapman D C. 1997. A simple theory for the fate of buoyant coastal discharges. Journal of Physical Oceanography, 27(7): 1386–1401, doi: 10.1175/1520-0485(1997)027<1386:ASTFTF>2.0.CO;2

Zeng Dingyong, Ni Xiaobo, Huang Daji. 2012. Temporal and spatial variability of the ZheMin Coastal Current and the Taiwan Warm Current in winter in the southern Zhejiang coastal sea (in Chinese). Scientia Sinica (Terrae), 42(7): 1123–1134, doi: 10.1360/zd-2012-42-7-1123

Zhang Caiyun, Huang Yan, Ding Wenxiang. 2020. Enhancement of Zhe-Min Coastal Water in the Taiwan Strait in winter. Journal of Oceanography, 76(3): 197–209, doi: 10.1007/s10872-020-00539-5

Zhang Caiyun, Shang Shaoling, Chen Dewen, et al. 2005. Short-term variability of the distribution of Zhe-Min Coastal Water and wind forcing during winter monsoon in the Taiwan Strait. Journal of Remote Sensing, 9(4): 452–458

Zhang Yinglong, Ye Fei, Stanev E V, et al. 2016. Seamless cross-scale modeling with SCHISM. Ocean Modelling, 102: 64–81, doi: 10.1016/j.ocemod.2016.05.002

Zhou Feng, Xue Huijie, Huang Daji, et al. 2015. Cross-shelf exchange in the shelf of the East China Sea. Journal of Geophysical Research: Oceans, 120(3): 1545–1572, doi: 10.1002/2014JC010567